Proceedings of the ASME 2023
International Design Engineering Technical Conferences and
Computers and Information in Engineering Conference
IDETC-CIE2023
August 20-23, 2023, Boston, Massachusetts

DETC2023-115071

TESTING AND VALIDATION OF A MOBILE DAMPING ROBOT FOR POWER LINES

Andrew Choi, Oumar Barry*

Department of Mechanical Engineering Virginia Polytechnic Institute and State University Blacksburg, Virginia 24061

ABSTRACT

Fixed passive vibration absorbers (FPVAs) are widely used on power lines and other continuous systems, but they are inherently limited since changes in wind conditions affect absorber performance due to changing mode shapes. A mobile damping robot (MDR) can overcome these limitations by actively transporting a passive absorber to conductor antinodes where the absorbers can most effectively remove energy from the system. While many analyses have been performed for fixed masses on power line conductors, they have not been in the context of interactions between the conductor and a mobile damping robot (MDR). There is a need to explore the potential impact of the MDR on the power line and the resulting implications for the MDR's development as current methods of vibration control do not adequately address fatigue failure caused by wind-induced vibrations (WIV). In this paper, we define a mathematical model of the system and perform numerical analysis in MATLAB® using equations of motion obtained via Hamilton's Principle. We investigate the adequacy of an experimental test bench for testing. Then we experimentally validate the ability of a mobile robot to transport a mass along a conductor to antinode locations. Experimental results indicate that the robot is able to navigate to the locations of highest amplitude on the cable. The insights gained from this work lay a foundation to guide future experiments that will better define the operating conditions of the MDR and lead to the creation of an appropriate control framework.

Keywords: vibration, vibration control, mobile robots

1 INTRODUCTION

Power transmission is critical to the nation's infrastructure, and its maintenance is a key priority, especially as the electric grid ages. However, current solutions do not adequately protect against structural damage caused by wind blowing across the conductor, exciting it, and causing it to vibrate. These wind-induced vibrations (WIV) are typically Aeolian vibrations caused by vortex shedding with frequencies in the range of 3-150 Hz and wind speeds of 1-7 m/s [1-7]. Over time, WIV can cause fatigue failure due to high cycles of bending stress [8–13]. Fixed passive vibration absorbers (FPVAs) are currently used to damp transmission line vibrations, thereby reducing amplitude in an effort to keep the cable below its endurance limit. [14–17]. However, FPVAs are fundamentally inefficient at certain resonance frequencies due to their inability to change location. Absorbers are maximally effective at dissipating energy when they are placed at cable antinodes, or locations of highest amplitude. However, the absorbers are rarely at these optimal locations. Although studies have been performed to optimize FPVA placement, it is not possible to place FPVAs near antinode locations for all resonance frequencies in the range of Aeolian vibrations [18–20]. Conversely, absorbers are least efficient at dissipating energy when they are placed at cable nodes, or locations of lowest amplitude. In fact, if the FPVA is fixed at a node, it may be worse than having no absorber at all due to the increased strain caused by the mass of the absorber [18, 20]. Although the odds of a fixed absorber's placement coinciding with the location of a node are low, the potential damage is quite high. Even low frequency vibrations for just minutes each day would result in several megacycles each year. An FPVA's effectiveness is further dependent on its ability to match the resonance frequencies of the conductor to which it is attached, typically being limited

^{*}Corresponding Author (Email: obarry@vt.edu)

to just a few matching frequencies [4, 14, 15, 20, 21].

To overcome these shortcomings, Barry et al [13] have proposed a novel mobile damping robot (MDR) for vibration control, as shown in Figure 1. While some researchers have previously explored the concept of moving dampers in other domains [22, 23], Barry et al were the first to investigate moving dampers in the context of power line WIV suppression [13]. Their MDR would be capable of adapting to changing wind characteristics to automatically re-position to the locations of antinodes. While other mobile power line robots have been developed, they suffer from significant drawbacks. For example, their high cost, heavy weight, and need for user input cause them to be unsuitable for long-term mounting on transmission lines. Moreover, these robots almost exclusively focus on inspection rather than active control and monitoring. The MDR fills this technology gap and is specifically designed for long-term mounting and autonomous suppression of cable vibrations. The MDR was further explored by Kakou et al, who utilized feedback control to adapt the MDR's motion profile to the current input excitation [24–26].



FIGURE 1: Conceptual design model of the mobile damping robot.

However, the previous work by Kakou et al required knowledge of the cable parameters and excitation frequency for the MDR to locate and travel to the theoretical antinode positions. Since the presence of the MDR on the conductor impacts cable dynamics, operation of the MDR based on theoretical knowledge would likely result in the robot traveling to an incorrect position in real-world situations. Therefore, a critical research need exists to examine how the presence of the MDR itself affects conductor vibrations and behavior, as well as the MDR's ability to adapt to shifting wind conditions in real-time. In this paper, we outline a mathematical model of the cable with an MDR. We define the experimental setup and validate the mathematical model numerically in MATLAB® Then we detail the operation of the MDR and validate its ability to navigate to cable regions of highest amplitude. In this work, for the first time, we demonstrate the ability of a mobile damping robot to navigate to the resultant antinodes of a power line conductor with no a priori knowledge. Finally, we discuss our findings and outline suggestions for future improvements and experiments to better develop the MDR.

2 MATHEMATICAL MODEL

A mathematical model of the system was used for analysis in MATLAB® and is depicted in Fig. 2. The conductor cable and MDR were modeled as forced vibration of a mass-spring-damper-mass system in keeping with previous work in the literature [19, 24, 26–28]. Here, x is the horizontal placement of the MDR on the cable span, m_i is the in-span robot mass, k is the spring constant of the absorber, c is the damping coefficient of the absorber m_d is the suspended absorber mass, and y_d is the vertical displacement of the suspended absorber mass.

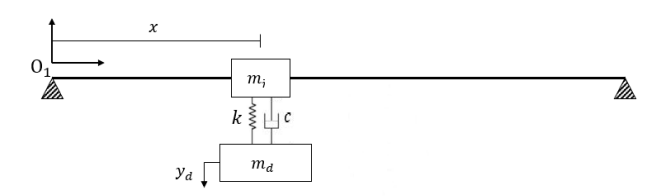


FIGURE 2: Schematic of the MDR on a conductor cable.

The conductor cable is modeled as a simply supported Euler-Bernoulli beam based on the parameters given in Table 1. While the flexural rigidity varies along the span, EI is typically low for most conductors and so does not greatly affect conductor motion. If the EI is quite small, the conductor can behave like a string [29]. Ordinarily, the small diameter of our conductor would cause us to assume a very small moment of inertia and, therefore, a very small flexural rigidity as well. However, in this case, the low tension of the experimental setup allows the EI term to dominate, making the beam model more accurate than the string model.

TABLE 1: Cable Parameters.

Parameter	Value	Unit
Mass	2.56	kg
Length	7.32	m
Tension	872	N
Diameter	1.44	ст
Elasticity	71	GPa

The position vectors of the beam, in-span mass, and suspended mass are first defined to represent their positions and displacements. The time derivatives of the position vectors are then derived and used to further derive the velocity vectors. The velocity vectors are used to find the kinetic energy of the system elements, the sum of which define the kinetic energy of the system as a whole. The potential energy is defined for the system elements with consideration of restoring forces. The application of Hamilton's Principle to these equations results in the following equation of motion

$$EIy'''' + m\ddot{y} + Ty'' = F(x,t) - (F_1 + F_2)D(x,t)$$
 (1)

Here F(x,t) is an excitation force at a single point expressed in the form of

$$F(t) = f_0 \sin(\omega_e t) \tag{2}$$

where f_0 is the amplitude of the force, and ω_e is the input frequency. F1, F2 and D(x,t) are expressed as

$$F_1 = m_i \ddot{y} \tag{3}$$

$$F_2 = k(y - y_d) + c(\dot{y} - \dot{y_d})$$
 (4)

$$D(x,t) = \delta(x - x_r) \tag{5}$$

Finally, the transverse displacement of the suspended mass is given to be

$$m_d \ddot{\mathbf{y}}_d - F_2 = 0 \tag{6}$$

3 EXPERIMENTAL TEST BENCH

3.1 Experimental Setup

The experiments were performed using an exciter (LDS Test and Measurement V408 electrodynamic shaker), an analyzer (Polytec), and a signal conditioner (Bruel & Kjaer LDS LPA100 amplifier). A scanning vibrometer (PSV-500-3D) was placed above the cable to scan multiple points across a full vibration loop of the mode shape corresponding to the forcing frequency. The instruments used are depicted in Figure 3. Additionally, an accelerometer (PCB Piezotronics 352C33) was used to measure the input acceleration of the shaker as a reference. Polytec PSV

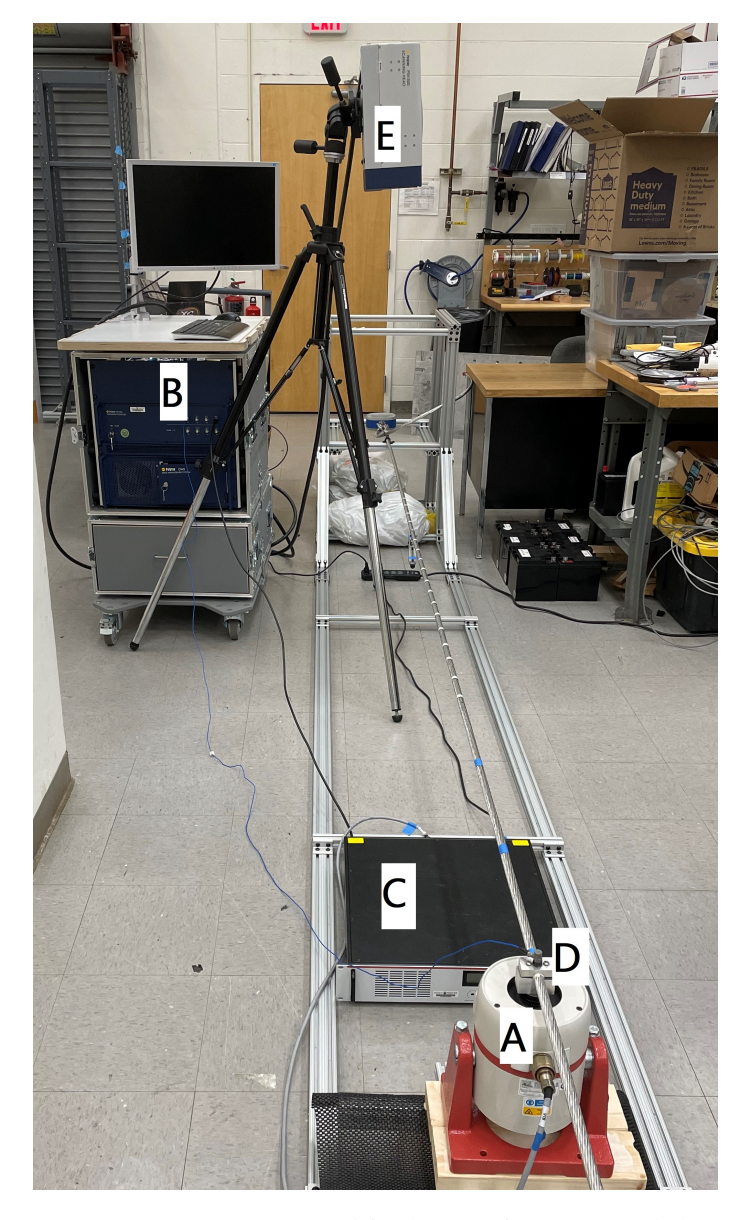


FIGURE 3: Instruments used in the experiments: A) Shaker, B) Analyzer, C) Amplifier, D) Clamp Connection, E) Scanning Head.

Software was used to interface with the hardware and record data.

Figure 4 depicts a representation of the full experimental test bench. Figure 5 depicts a representation of the portion of the experimental test bench used for testing at the 8th harmonic. The 8th mode was selected for the experiment since it best fit the constraints of the experimental setup while avoiding the pitfalls of earlier experiments. In particular, the 8th harmonic was desirable due to accessible non-bounded vibration loops with lengths of nearly a meter. We used one half of the cable for testing due to

the placement of the shaker at midspan. This configuration produced the most equal vibration loops at roughly 0.92 m each between two adjacent nodes. Loops 2 and 3, between N2 & N3 and N3 & N4 respectively, were used for testing. To avoid unwanted boundary conditions, we excluded the first and fourth loops from testing.

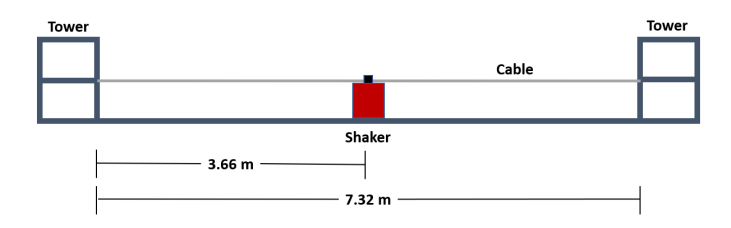


FIGURE 4: Representation of the experimental setup.

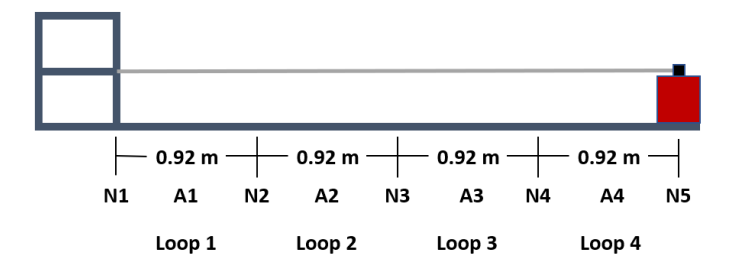


FIGURE 5: Representation of the portion of the experimental setup used for testing. Nodes are denoted with an 'N' and antinodes are denoted with an 'A'. Loops are bounded by nodes.

3.2 Test Bench Improvements

The experimental test bench was completely redesigned from previous experiments due to poor validation between numerical and experimental results [30]. This inconsistency was largely attributed to 1) a relatively short cable span, and 2) a relatively small cable diameter. The short span necessitated that previous testing was performed at low harmonics (3rd mode was predominantly tested) to ensure a large enough vibration loop length for testing. This meant that there were non-ideal boundary conditions and that certain nodes were unavailable for measurement due to serving as attachment points. The small diameter meant that the cable mass was also low, which would negatively impact the design of the MDR.

The full physical setup is shown in Figure 6 and entailed securing the cable to two towers using p-clamps and two-hole straps. A Haul-Master hand winch was used to tension the cable to 872 N, as measured using a PCE-CS 300 force gauge. The towers were constructed using T-slot aluminum framing, and the cable was a Sneezewart All Aluminum Conductor (AAC) with the parameters previously given in Table 1 in Section 2. The shaker was

rigidly attached to the cable at midspan with a clamp. The design was intentionally modular, such that the span length, cable height, and cable diameter can all be scaled as needed.



FIGURE 6: Experimental test bench.

3.3 Test Bench Validation

Both white noise excitation and a swept sine output were used to obtain the frequency response of the cable across a range of 0-200 Hz with a step increment of 0.1 Hz for the sweep. Resonance in the frequency response functions were best seen at the lower harmonics in the range of 0-20 Hz; however, the fundamental frequency and the second harmonic were deemed untrustworthy due to the limitations of the shaker operation below 10 Hz. After getting some measurements from random points along the conductor by a sine-sweep test, we found that an eighth harmonic

of the full conductor was at 32 Hz, which was easily verified by visual observation. When evaluated at a forcing frequency of 32 Hz, the cable vibrated at high amplitude and clearly demonstrated an eighth mode shape.

We initially tested the bare conductor with the sine output at 32 Hz, corresponding to the previously selected 8th mode shape. The scanning head vibrometer was placed above the cable to measure the velocity at nine points along the third loop. The response of the cable was displayed in PSV Acquisition with the magnitude of the velocity in mm/s as shown in Figure 7. Here, the leftmost point is toward the tower, and the rightmost point is toward the shaker at midspan. The areas between measurement locations were automatically interpolated by the PSV software. The region near the center of the loop showed high velocity as expected for an antinode region. Similarly, the node regions at the ends of the loop showed low velocity. This was also performed for the second loop to similar results.

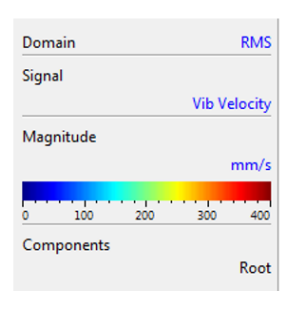


FIGURE 7: Velocity for the third loop of the cable without any mass attached. Dark blue denotes low magnitude and dark red denotes high magnitude.

When using stand-in masses for the robot, we found that the cable dynamics changed in accordance with our expectations, as shown in Figure 8. The velocity profile changed with the addition of a mass representing 15% (383g) of the cable mass. These results agree with our previous research on the effect of untuned masses [30], where we saw vibration loop lengths change in size with the addition of a mass. The nature of these changes were based on the value of the mass and its position. There, we observed that the addition of a mass to the vibration loop caused the nodes to shift inward toward the antinode, which aligned with our numerical findings. Each increase in mass coincided with an increased shrinking effect.

With the investigative ability of the PSV Acquisition equipment, we were able to document a decrease in velocity across the cable with a lower maximum velocity and an enlarged region

of minimum velocity. By moving the scanning head further toward midspan, we did find that there was also an enlarged region of maximum velocity. Therefore, the results indicate that the addition of a suspended mass both influences loop lengths as previously seen while also expanding the relatively discrete points of antinode and node locations to broader regions of maximum and minimum amplitude. These results were consistent for all three tested masses corresponding to approximately 5% (132g), 15% (383g) and 25% (640g) of the cable mass. A maximum of 25% was used to prevent the introduction of undesirable static deflection. One of the suspended masses used is shown in Figure 9.

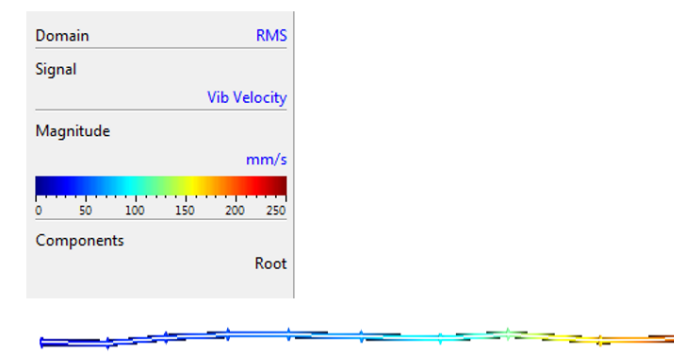
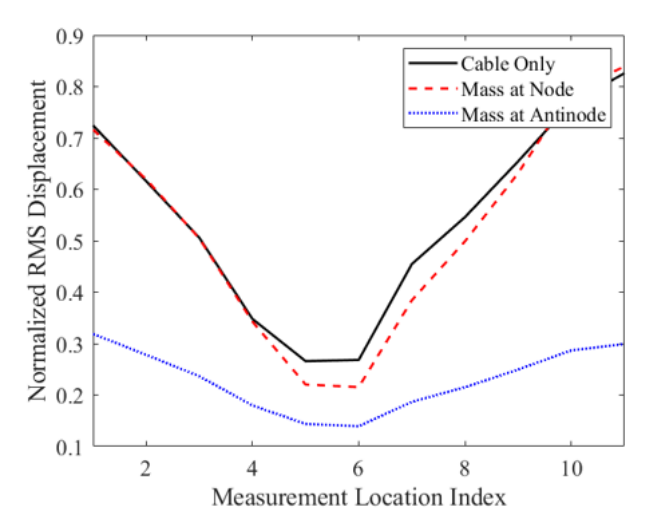


FIGURE 8: Velocity for the same cable segment with a mass corresponding to 15% of the cable mass attached at an antinode (A3). Dark blue denotes low magnitude and dark red denotes high magnitude.



FIGURE 9: Mass suspended on the cable.

Additional investigations were performed with the 15% mass attached at both the theoretical node and antinode locations. Tests were performed for ten harmonics from the 3rd mode to the 12th mode. The first and second modes were excluded due to both the limitations of the shaker and the inaccessibility of node and antinode locations for mounting the mass. Eleven points were measured along the same section of cable for all of the tests. Figure 10a shows the results at the 4th mode, which most clearly



(a) Experimental normalized RMS displacement for the 4th mode at 16 Hz.

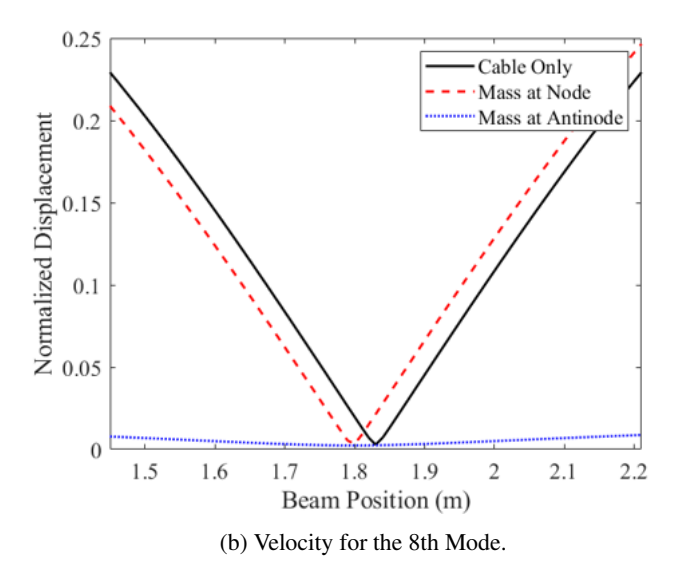
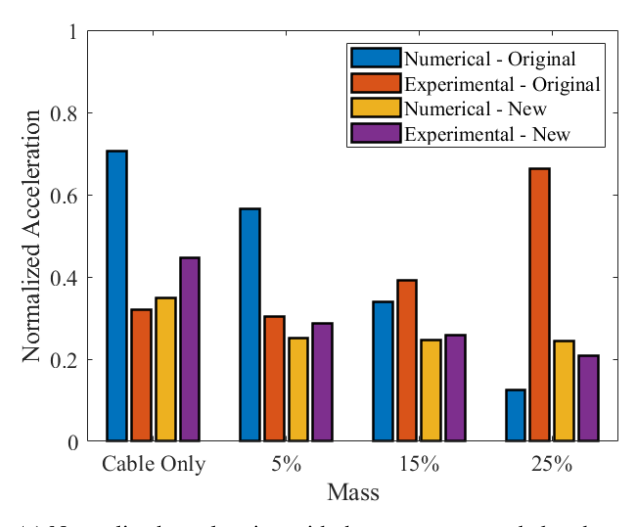


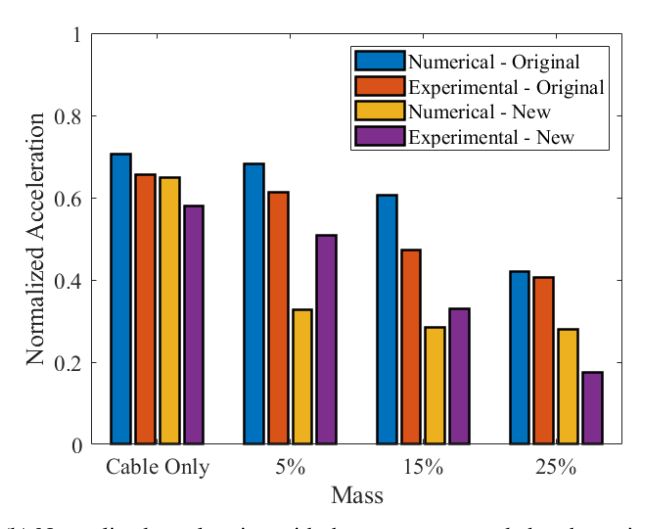
FIGURE 10: Numerical normalized RMS displacement for the same location of the cable at the 4th mode.

demonstrated the effects of the suspended mass. Mounting the mass at an antinode location had a clear positive effect on vibration reduction. As expected, the introduction of the suspended mass also changed the locations of the antinodes due to its impact on the cable dynamics. As such, it was known prior to testing of the robot prototype that the robot would not be navigating to the theoretical antinode position but would adapt to the changes in the cable.

These results were compared against the numerical results in MATLAB®, shown in Figure 10b. The ODE45 function was used to simulate the displacement of the cable and suspended



(a) Normalized acceleration with the masses suspended at the node.



(b) Normalized acceleration with the masses suspended at the antinode.

FIGURE 11: Comparison of the acceleration trends between test benches.

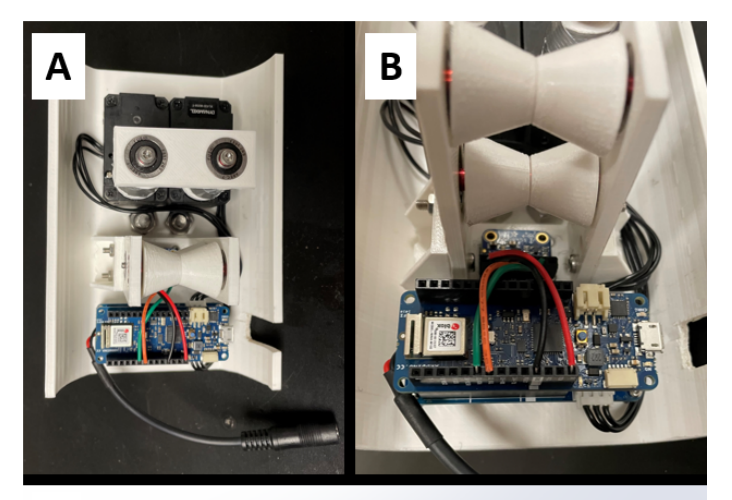
mass. The magnitude of the displacement was normalized since the particular experimental values were dependent on the gain settings of the amplifier. The position is given in meters and aligns with the measurement location in Figure 10a. There is an overall agreement in general trends between the experimental and numerical results. Adding the mass at the position of an node did not significantly change the displacement from those of the cable alone. Conversely, adding the mass at the position of an antinode did significantly change the displacement to be well below the those of the cable alone. However, the fidelity of the model was limited by the use of the mode shapes for the bare conductor. Even so, these results were notably better than those

found on the previous test bench despite using the same mathematical model. Evaluation of a string model was also performed, to worse results.

Figure 11 shows a comparison of the acceleration trends when the masses were placed at the nodes and antinodes. There is a clear contrast in agreement of results from the original test bench to the updated one. The original test bench saw a mismatch between the experimental and numerical results for the mass at the node. With the updated test bench, we saw agreements for this case, as well as with the mass at the antinode. These results indicated that the improved test bench was better suited for experiments, as it better aligned with the Euler-Bernoulli beam model. This was an important finding, as that mathematical model presented earlier in Section 2 has been well established in the literature for transmission lines commonly used in industry.

4 TESTING & RESULTS

4.1 MDR Prototype



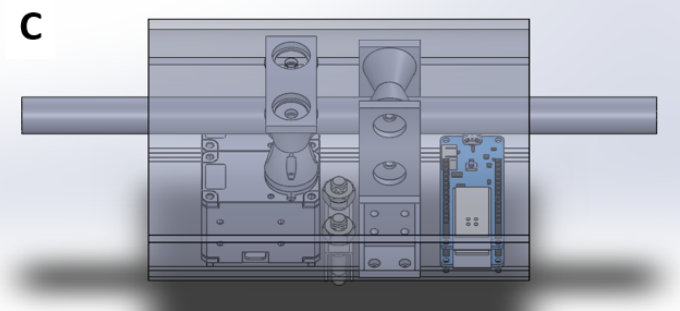


FIGURE 12: MDR tets prototype. A) Top level view of the motors, drive wheels, rollers, and microcontroller. B) Front view of the rollers, accelerometer, and microcontroller. C) Side view of the CAD model.

The test prototype for the MDR was comprised of an Arduino MKR Wifi 1010, an Adafruit MMA8451 triple-axis accelerometer, two Dynamixel XL430-W250-T servo actuators, a Dynamixel Shield for the Arduino, and 3D printed PLA (polyactide) components. The test prototype is shown in Figure 12. The Arduino was used for ease of programming and the widespread availability of compatible peripheral equipment. Dynamixel motors were used because while unnecessary for this stage of testing, their native ability for feedback control of velocity and position are desirable for future work. Similarly, a Wifi capable module was used to easily incorporate future data transmission capabilities.

4.2 Antinode Tracking Algorithm

The antinode tracking is implemented via an iterative improvement local search algorithm. A single acceleration value is saved at any given time, and the robot acts to improve the value with each iteration until it finds the highest value. A high level overview of the control algorithm is depicted in Figure 13. In this case, an initial accelerometer sample is taken, and the absolute maximum magnitude is determined. Then, the robot moves a predefined distance, whereupon it takes another sample. The absolute maximum of the new sample is compared to the absolute maximum of the initial sample. If the acceleration has increased, the robot will continue in the same direction toward the region of maximum amplitude. If the acceleration has decreased, the robot will reverse direction, again toward the region of maximum amplitude. The robot continues this cycle of sample, travel, compare until it reaches a position where the acceleration has not changed significantly from the previous position, as defined by a set threshold. There is also a counter to prevent continuous oscillation. Either condition indicates the successful navigation of the robot to the rough location of the antinode. The MDR prototype on the cable is shown in Figure 14

The accuracy of the robot to the antinode is theoretically within 2.54 cm as this is half the predefined travel distance of the robot between sample locations. Given a loop length of 0.92 m, this represents a positional accuracy of 2.7%. The accuracy could potentially be further increased by decreasing the step distance, but may result in an inability to reach the antinode due if the acceleration at adjacent locations are too similar and the threshold is not reached. To prevent unnecessary oscillation and incorrect values, several safeguards were put into place. First, the robot was programmed to take 100 samples to ensure the maximum acceleration value was found. A delay of two seconds was implemented after locomotion before a new sample to allow the transient response to settle. The robot was programmed to take larger steps than necessary to ensure significant differences in acceleration values between locations. Lastly, the threshold value was tuned based on the signal gain.

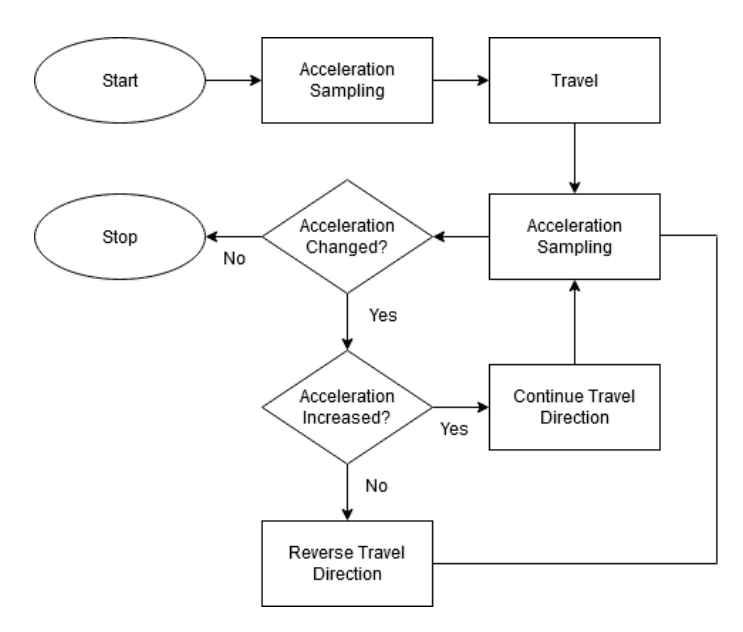


FIGURE 13: Overview of Antinode Tracking Algorithm.



FIGURE 14: MDR Prototype mounted on the test cable during experimental validation of the antinode tracking algorithm.

4.3 Results

The testing demonstrated that the MDR prototype was able to successfully navigate to a region of highest amplitude corresponding to the antinode, as verified by the scanning head. As previously noted in Section 3.3, this was not the same as the theoretical antinode location due to the changing cable dynamics and was also an elongated band rather than a discrete point. Additional testing was performed at 36 Hz (9th mode shape) for both Loops 2 and 3. This did not impact the ability of the robot to navigate to the regions of highest amplitude. Additional tests were also performed with different gains, and the MDR prototype was again able to navigate to the antinode regions once the threshold value was appropriately tuned.

5 CONCLUSION & FUTURE WORK

The numerical analysis demonstrated that for our experimental setup, a beam model is more appropriate than a string model, as

the numerical analysis showed agreement with the experimental findings under a beam model. We also validated the new experimental test bench as superior to the previous design. Even so, more precise modeling could be achieved by incorporating nonlinear effects. Testing should also be performed in a wind tunnel with an accompanying change to the model to simulate a uniformly distributed wind force composed of various frequencies. The test bench could also be improved by using a larger diameter cable with steel reinforcement to further increase the dominance of the *EI* term.

The testing of the MDR prototype on the cable demonstrated that the robot was able to navigate to the regions of highest amplitude under various excitation conditions. We note that these regions were not discrete points but elongated bands of high amplitude. These results indicate that the antinode algorithm can effectively track the vibration antinode as desired. We also found that the MDR helped reduce the average vibration of the system for different resonant frequencies, even with untuned masses. This is consistent with previous results and suggests that the MDR should have a positive impact on conductor vibration even when the suspended vibration absorber is not tuned to a given resonance frequency of the conductor.

To further improve the MDR's performance, we will assess the cable response with tuned absorbers and test at additional frequencies. We will also adjust the placement of the electrodynamic shaker and perform testing of the robot at various points along the cable while excitation conditions change. The algorithm with be commensurately tuned to be more adaptive to such changes, as well as designed for increased robustness through boundary setting, incorporation of additional sensors, dynamic parameter setting, and exploration of transmissibility.

ACKNOWLEDGMENTS

This work is funded by National Science Foundation CA-REER Award ECCS 1944032: Towards a Self-Powered Autonomous Robot for Intelligent Power Lines Vibration Control and Monitoring. Any opinions, findings, and conclusions or recommendations expressed in this material are those of the author(s) and do not necessarily reflect the views of the National Science Foundation.

REFERENCES

[1] Oumar Barry, Donatus CD Oguamanam, and Der Chyan Lin. Aeolian vibration of a single conductor with a stockbridge damper. *Proceedings of the Institution of Mechanical Engineers, Part C: Journal of Mechanical Engineering Science*, 227(5):935–945, 2013.

- [2] Morteza Sadeghi and Aryo Rezaei. Aeolian vibrations of transmission line conductors with more than one damper. *International Journal of Engineering*, 28(10):1515–1524, 2015.
- [3] Kunpeng Ji, Bin Liu, Jingchao Wang, Peng Li, Danyu Li, Lichun Zhang, Jingshan Han, and Yifeng Wang. Aeolian vibration and its suppression methods of long crossing span overhead electric transmission line. In 2019 6th International Conference on Information Science and Control Engineering (ICISCE), pages 663–667. IEEE, 2019.
- [4] Rafiou Oumar Barry. *Vibration Modeling and Analysis of a Single Conductor With Stockbridge Dampers*. PhD thesis, University of Toronto, 2014.
- [5] Suzanne Guerard, Bertrand Godard, and Jean-Louis Lilien. Aeolian vibrations on power-line conductors, evaluation of actual self damping. *IEEE transactions on power delivery*, 26(4):2118–2122, 2011.
- [6] O Barry, JW Zu, and DCD Oguamanam. Analytical and experimental investigation of overhead transmission line vibration. *Journal of Vibration and Control*, 21(14):2825– 2837, 2015.
- [7] Chiara Gazzola, Francesco Foti, Luca Martinelli, and Federico Perotti. An appraisal of modelling strategies for assessing aeolian vibrations of transmission lines. In 24th Conference of the Italian Association of Theoretical and Applied Mechanics, AIMETA 2019, pages 1522–1534. Springer, 2020.
- [8] GE Braga, R Nakamura, and TA Furtado. Aeolian vibration of overhead transmission line cables: endurance limits. In 2004 IEEE/PES Transmision and Distribution Conference and Exposition: Latin America (IEEE Cat. No. 04EX956), pages 487–492. IEEE, 2004.
- [9] YD Kubelwa, RC Loubser, and P Moodley. Experimental investigations of bending stresses of acsr conductors due to aeolian vibrations. In *Cigre Science & Engineering*, volume 9, pages 1286–1146. Innovation in the power systems industry, 2017.
- [10] Suzanne Guérard, Jean-Louis Lilien, et al. Evaluation of power line cable fatigue parameters based on measurements on a laboratory cable test span. In *EIght International symposium on Cable Dynamics, ISCD 2009*, page 125. AIM, rue St Gilles, 31, 2009.
- [11] CBSInternational Journal of Mechanical Sciences. 4,000 dte customers remain without power nearly a week after damaging winds. 1:163–178, 2017.

- [12] President's Council of Economic Advisers. Economic benefits of increasing electric grid resilience to weather outages. 1:163–178, 2013.
- [13] Oumar Barry and Mohammad Bukhari. On the modeling and analysis of an energy harvester moving vibration absorber for power lines. In *Dynamic Systems and Control Conference*, volume 58288, page V002T23A005. American Society of Mechanical Engineers, 2017.
- [14] NK Vaja, OR Barry, and EY Tanbour. On the modeling and analysis of a vibration absorber for overhead powerlines with multiple resonant frequencies. *Engineering Structures*, 175:711–720, 2018.
- [15] Oumar Barry, JW Zu, and DCD Oguamanam. Nonlinear dynamics of stockbridge dampers. *Journal of Dynamic Systems, Measurement, and Control*, 137(6):061017, 2015.
- [16] Nitish Kumar Vaja, Oumar Barry, and Brian DeJong. Finite element modeling of stockbridge damper and vibration analysis: Equivalent cable stiffness. In *International Design Engineering Technical Conferences and Computers and Information in Engineering Conference*, volume 58226, page V008T12A012. American Society of Mechanical Engineers, 2017.
- [17] Oumar Rafiou Barry, Emadeddin Y Tanbour, Nitish Kumar Vaja, and Hesham Tanbour. Asymmetric aeolian vibration damper, April 17 2018. US Patent 9,948,081.
- [18] A Rezaei and MH Sadeghi. Analysis of aeolian vibrations of transmission line conductors and extraction of damper optimal placement with a comprehensive methodology. *International Journal of Engineering*, 32(2):328–337, 2019.
- [19] O Barry, R Long, and DCD Oguamanam. Simplified vibration model and analysis of a single-conductor transmission line with dampers. *Proceedings of the Institution of Mechanical Engineers, Part C: Journal of Mechanical Engineering Science*, 231(22):4150–4162, 2017.
- [20] ML Lu and JK Chan. An efficient algorithm for aeolian vibration of single conductor with multiple dampers. *IEEE Transactions on power Delivery*, 22(3):1822–1829, 2007.
- [21] US EPRI and EDF R&D. Profiling and mapping of intelligent grid r&d programs. Technical report, Palo Alto, CA: US EPRI, 2006.
- [22] Jixiong Fei, Bin Lin, Shuai Yan, Mei Ding, Juliang Xiao, Jin Zhang, Xiaofeng Zhang, Chunhui Ji, and Tianyi Sui. Chatter mitigation using moving damper. *Journal of Sound and Vibration*, 410:49–63, 2017.
- [23] YR Wang and CY Lo. Design of hybrid dynamic balancer and vibration absorber. *Shock and Vibration*, 2014, 2014.

- [24] Paul Kakou, Mohammad Bukhari, Jiamin Wang, and Oumar Barry. On the vibration suppression of power lines using mobile damping robots. *Engineering Structures*, 239:112312, 2021.
- [25] Paul-Camille Kakou. *Towards A Mobile Damping Robot For Vibration Reduction of Power Lines*. PhD thesis, Virginia Tech, 2021.
- [26] Paul-Camille Kakou and Oumar Barry. Toward a mobile robot for vibration control and inspection of power lines. ASME Letters in Dynamic Systems and Control, 2(1):011001, 2021.
- [27] O Barry, JW Zu, and DCD Oguamanam. Forced vibration of overhead transmission line: analytical and experimental investigation. *Journal of Vibration and Acoustics*, 136(4), 2014.
- [28] Mohammad A Bukhari and Oumar R Barry. Nonlinear vibrations analysis of overhead power lines: A beam with mass–spring–damper–mass systems. *Journal of Vibration and Acoustics*, 140(3), 2018.
- [29] Jack Vecchiarelli. *Aeolian vibration of a conductor with a Stockbridge-type damper*. PhD thesis, 1998.
- [30] Andrew Choi, Paul-Camille Kakou, and Oumar Barry. Considerations for the testing and validation of a mobile damping robot for overhead power lines. In *International Design Engineering Technical Conferences and Computers and Information in Engineering Conference*, volume 86311, page V010T10A026. American Society of Mechanical Engineers, 2022.